Modeling the Effects of Drift Orbit Bifurcation on Radiation Belt Electrons

Jinbei Huang[1], Weichao Tu[1], W. W. Eshetu[1]

[1]Department of Physics and Astronomy, West Virginia University, Morgantown, WV, USA

Key points:

- Test particle simulations are performed to quantify the effects of drift orbit bifurcation on radiation belt electrons.
- Short-term simulations after one drift show electron transport due to both traditional and nontraditional drift orbit bifurcation.
- Long-term transport coefficients by drift orbit bifurcation could be comparable to or larger than those by wave-particle interactions.

Abstract

Drift Orbit Bifurcation (DOB) has been suggested to play a major role in the loss and transport of radiation belt electrons since it violates the second and third adiabatic invariants of particles. Results from our guiding-center test particle simulations using the Tsyganenko-1989c magnetic field model show that the DOB could affect a broad region of the outer radiation belt, which can penetrate inside the geosynchronous orbit at $Kp \geqslant 3$, and its effects are more significant further away from Earth, at higher *Kp*, and for higher electron energies. Specifically, the short-term simulation results after one electron drift show both traditional and nontraditional DOB transport of electrons, with the nontraditional DOB, caused by a third minimum of the magnetic field strength near the equator, reported here for the first time. Moreover, our results show large ballistic jumps in the second invariant and radial distance for electrons at high equatorial pitch angles after one drift. In addition, long-term DOB transport coefficients of electrons over many drifts are calculated based on our simulation results. We find that the pitch angle and radial diffusion coefficients of electrons due to DOB could be comparable to or even larger than those caused by electron interactions with chorus and ULF waves, respectively. In sum, our results demonstrate that DOB could cause effective loss and transport of radiation belt electrons even in the absence of waves.

1. Introduction

Earth's radiation belts contain energetic electrons and protons that present a hazardous radiative environment for spacecraft (e.g., Baker, 2001; Allen, 2010). The relativistic electrons in the radiation belts are characterized by large variations in flux on various time scales (Reeves et al.,

2003; Baker & Kanekal, 2008). Recently, the NASA Van Allen Probes mission revealed two types of remarkable variations of outer belt electrons: the strong enhancement and the fast dropout of electron flux by orders of magnitude on timescales of a few hours. Significant progress has been achieved in understanding the strong enhancement of relativistic electrons, which can be well reproduced by local acceleration from chorus waves based on realistic wave and plasma conditions (e.g., Thorne et al., 2013; Tu, Cunningham, et al., 2014). However, the fast dropout of relativistic electrons has not been well studied, which remains as one of the most compelling and outstanding questions in Earth's radiation belt studies. During the fast dropout, radiation belt electrons can be lost either by transport across the magnetopause into interplanetary space, called magnetopause shadowing, or by precipitation into the atmosphere. Precipitation is generally considered to be caused by wave-particle interactions that induce pitch angle diffusion of electrons (Thorne, 2010, and references therein). Magnetopause shadowing occurs either due to the solar wind compression of the magnetopause or the outward radial transport of electrons. The latter is commonly attributed to the electron outward radial diffusion driven by Ultra-Low-Frequency (ULF) waves (Fälthammar, 1965; Turner et al., 2012). Even though these traditional loss mechanisms have been extensively included in radiation belt models to simulate the fast electron dropouts, in many cases, the observed dropouts still cannot be fully explained (Albert, 2014, and references therein). For example, to simulate the rapid loss of MeV electrons across the entire outer belt during the October 2012 storm, Tu, Cunningham, et al. (2014) applied the DREAM3D diffusion model, which includes pitch angle diffusion, radial diffusion, and the event-specific last closed drift shell of electrons to physically account for the magnetopause shadowing loss. However, the simulated loss did not penetrate as deep in L^*, the third adiabatic invariant (Roederer, 1970), as in the observations, and the large dropout at $L^* > 4$ was not sufficiently reproduced. Similarly, using a radial diffusion model with

data-driven outer boundary and electron losses from wave scattering, Ozeke et al. (2017) well explained the long-lasting ($\geq$ 10 days) feature of the ultra-relativistic electron depletion in September 2014. However, the rapid electron dropout that initiated the long-term depletion remains unsolved. In many cases, the dropouts are observed to cover a wide range of L (L is the equatorial distance in the Earth radii) shells, electron energies, and pitch angles, which cannot be fully explained by even combing all the traditional mechanisms.

Recent studies suggested that an anomalous process called Drift Orbit Bifurcation (DOB) can significantly affect the loss and transport of radiation belt electrons (e.g., Öztürk & Wolf, 2007; Wan et al., 2010; Ukhorskiy et al., 2011, 2014, 2015). DOB occurs when the dayside magnetosphere is compressed by the solar wind, exhibiting two local magnetic field minima on either side of the equator. The magnetic field strength distribution along the compressed field lines shows a W-shape instead of a U-shape. When particles traverse the dayside compressed W-shape region, i.e., the bifurcation region (Öztürk & Wolf, 2007), they could be temporarily trapped in one of the hemispheres off the equator when the magnetic field strength at the local maximum at the equator is bigger than B_m, the magnetic field strength at the particle's mirror points. Particles will resume bouncing across the equator when they drift away from the bifurcation region. The first adiabatic invariant, $\mu = mv^2\gamma^2/2B_m$, and B_m are constant during the DOB process. However, the second adiabatic invariant, $J = \oint p_{\parallel} ds = 2pI$, is violated when the particles are close to the bifurcation lines (Öztürk & Wolf, 2007), where the local B maximum at the equator is equal to B_m. Here p is the particle momentum and $p_{\parallel}$ is the momentum parallel to the local magnetic field. $I = \int_{-s_m}^{s_m} \sqrt{1 - B(s)/B_m} ds$ is usually used as the second adiabatic invariant of motion (rather than J) as it is only related to the geometry of the magnetic field. Here B(s) is the magnetic field strength

along the field line, s_m and $-s_m$ are the locations of the mirror points, and the integration is along the bounce trajectory of the particle. Since I is not conserved during the DOB process, the drift shell is not closed and the third adiabatic invariant, Φ or L^*, is undefined.

Many theoretical and numerical studies have been performed to quantify the jump of the second adiabatic invariants due to DOB. For example, Öztürk and Wolf (2007) used the separatrix crossing theory (Cary et al., 1986) and theoretically derived the jump of the second adiabatic invariant, ΔI, at the bifurcations. Then by calculating the ensemble average of ΔI over particle bounce phases, they identified two regimes of particle transport: a diffusive regime, where $\langle \Delta I \rangle \approx 0$ and $\langle (\Delta I)^2 \rangle \neq 0$, for particles starting with large I values and a ballistic or advective regime, where $\langle \Delta I \rangle > 0$, for particles starting with small I values. For simplicity, their derivations are based on the north-south and east-west symmetry of the magnetic field. For the field lacking such symmetry, Wan et al. (2010) found much larger transport rates using a semi-numerical approach. On the other hand, since particles are subject to phase mixing after multiple bifurcations, it is critical to quantify the statistical invariant transport over many drift orbits. Ukhorskiy et al. (2011) performed test particle simulations of DOB and found that the long-term evolution of I for electrons due to multiple DOB is a complicated interplay of both diffusion and advection processes.

The violation of both I and L^* during the DOB process can lead to radial transport of electrons for them to be lost through the magnetopause. For example, based on a 3D test particle approach, Ukhorskiy et al. (2014) found that the radial transport rates caused by DOB can exceed the transport rate driven by ULF waves by an order of magnitude. Later they applied a similar test particle code to simulate the global outer belt dropout observed during the March 2013 event (Ukhorskiy et al., 2015). Their results showed that DOB accounts for about 60% of the radial

transport above $L = 5$, leading to fast loss to the magnetopause. Additionally, even though DOB is considered most efficient near the dayside magnetopause, Ukhorskiy et al. (2011) show that a broad range of outer belt drift shells is susceptible to DOB, even during quiet solar wind conditions.

Therefore, even though DOB has been suggested to significantly contribute to the loss and transport of radiation belt electrons, its effects have not been sufficiently explored and quantified. Moreover, the relative importance of DOB to the loss and transport of radiation belt electrons is not yet understood. To better understand the DOB effects, in this work we quantify electrons' short-term and long-term transport due to DOB under different geomagnetic conditions, which could be applied to global radiation belt modeling in the future. We also investigate the energy dependence of the electron DOB transport and the nontraditional DOB effects due to three local magnetic field minima which is reported here for the first time. Section 2 introduces the methodology and particle setup for the 3-D test particle simulations. Section 3 shows the simulation results for the short-term transport of electrons due to DOB after one full drift, including the nontraditional type of DOB effects due to three local B minima, and the long-term transport rates of electrons due to DOB after many drifts. Section 4 finishes with conclusions and discussions.

2. Test Particle Simulation

Since the first adiabatic invariant is conserved in DOB, we use the guiding center equations by Brizard and Chan (1999) to track the guiding center trajectories of electrons:

$$\begin{cases} \dfrac{d\vec{R}}{dt} = \dfrac{p_{\parallel}}{\gamma m}\dfrac{\vec{B}^*}{B_{\parallel}^*} + \dfrac{\mu}{\gamma q}\dfrac{\hat{b}\times\nabla B}{B_{\parallel}^*}, \\ \dfrac{dp_{\parallel}}{dt} = -\dfrac{\mu}{\gamma}\dfrac{\vec{B}^*\cdot\nabla B}{B_{\parallel}^*}, \end{cases} \tag{1}$$

where $\vec{B}^* = \vec{B} + (p_{\parallel}/q)\nabla \times \hat{b}$, $\hat{b}$ is the unit vector of $\vec{B}$, $\vec{R}$ is the electron guiding center position, $p_{\parallel}$ is the parallel momentum of the electron, γ is the Lorentz factor, m and q are the mass and charge of the electron, and μ is the first adiabatic invariant. These guiding center equations, which can be efficiently solved numerically and perform well in conserving the energy and adiabatic invariants of particles, have been widely used to investigate the effects of DOB on particles (e.g., Ukhorskiy et al., 2011, Wan et al., 2010). In our simulations, the fourth-order Runge-Kutta method is used to solve the guiding center equations numerically. We have chosen the T89c magnetic field model (Tsyganenko, 1989) for simulations as it is solely controlled by the geomagnetic *Kp* index, which makes the quantified transport rate of electrons (discussed in Section 3.3) easier to be parametrized for future application in global radiation belt models. The simulations are performed in static magnetic field conditions (i.e., given *Kp* levels) with no induced electric field to isolate the DOB effects due to magnetic field geometries. We have also set a zero-tilt angle of the Earth's intrinsic dipolar magnetic field in the GSM coordinates. The lower boundary of the model is set at 100 km altitude, which is the general height of the Earth's atmosphere. As there is no explicitly defined realistic magnetopause in the T89c magnetic field, we set the upper boundary as 20 times Earth's radius. If the radial distance of the particle's guiding center is out of the boundary, we assume the particle is lost.

In our simulations, we investigate the DOB effects at different geomagnetic conditions (*Kp* = 1, 3, 6) for electrons starting from various radial distances from Earth with different values of initial second adiabatic invariants (I_0), and at different energies (E = 1, 2, 4 MeV). The electrons' guiding centers are initiated from the midnight meridian with different L_M, which is the radial distance from Earth of the midnight guiding center at the magnetic equator. To further study the bounce phase dependence, the electrons' guiding centers are separated at a uniform distance along the

initial guiding magnetic field line at midnight with a given L_M. These electrons are in different bounce phases with different local pitch angles but with the same equatorial pitch angles. Then we use the guiding center equations listed above to track the trajectory of each electron's guiding center. Our simulation results for the short-term and long-term electron transport due to DOB are discussed in the next section.

3. Simulation Results

3.1 Traditional and Nontraditional DOB

For the short-term transport of electrons due to DOB, Figure 1 shows the distribution of the calculated second adiabatic invariant after one full drift of electrons from the simulations, I_1, vs. the initial second adiabatic invariant, I_0, for electrons under different conditions. The initial equatorial pitch angle, α_{eq}, of electrons corresponding to the initial I_0 values are also denoted along the x-axis. Figure 1a is for 1 MeV electrons starting from the guiding field line at midnight with $L_{M0} = 6.8$ under $Kp = 3$. For each I_0 value 201 electrons with different bounce phases are simulated, with each black asterisk in the plot representing one electron. The results show that the electrons with different bounce phases can result in different changes of the second adiabatic invariant due to DOB. The thick red line shows the averaged value of I_1 over all the 201 electrons at different bounce phases, and the thin cyan line marks the y = x line as a reference. Based on the simulation results, we calculate the change of the second adiabatic invariant, $\Delta I = I_1 - I_0$, for each electron and then the bounce averaged values of $\langle \Delta I \rangle$ and $\langle (\Delta I)^2 \rangle$ for all the electrons at the same initial I_0. As discussed in Section 1, previous results have shown that the short-term transport of electrons

due to DOB can be identified as two regimes: a diffusive regime, with $\langle \Delta I \rangle \approx 0$, $\langle (\Delta I)^2 \rangle \neq 0$, for particles starting with large I values and a ballistic or advective regime, with $\langle \Delta I \rangle > 0$, for particles starting with small I values (Öztürk & Wolf, 2007). Our simulations results shown in Figure 1a are consistent with the previous findings, with the red curve generally above the cyan y = x line (i.e., $\langle \Delta I \rangle > 0$) at smaller I_0 and aligning with the y = x line at larger I_0 values (i.e., $\langle \Delta I \rangle \approx 0$). Specifically, to define a clear cut between the ballistic and diffusive regions, we compare the values of $\langle \Delta I \rangle$ and $\langle (\Delta I)^2 \rangle$ by calculating the ratio of $\langle \Delta I \rangle / \langle (\Delta I)^2 \rangle^{1/2}$. As I_0 increases from 0 in the plot, we choose the first I_0 value with $\langle \Delta I \rangle / \langle (\Delta I)^2 \rangle^{1/2} < 50\%$ as the boundary between the ballistic and the diffusive regimes, as marked by the first dashed blue line in the plot. This definition works well to separate the ballistic and diffusive regimes in our simulation results, with more examples shown in Figure 5, which will be discussed later. Based on our simulation results, we can also mark the boundary between the diffusive and the adiabatic regimes as the second dashed blue line in the plot. The adiabatic regime is defined as the regime where no bifurcation occurs, as shown in the simulation results.

The results plotted in Figure 1a are consistent with previous findings of the short-term transport of electron I values due to DOB, which is called traditional DOB in this paper. To better illustrate the change of I during the electron's drift for traditional DOB, we select three cases to represent the electron transport in different regimes, as marked as (A), (B), and (C) in Figure 1a, and illustrate their DOB transport in Figure 2 panels (a-c). Each row of Figure 2 shows the change of magnetic field profiles along the field line, with the equator in the center, over one drift period of the electron, from midnight to prenoon, noon, afternoon, then back to midnight. The red lines represent the electron's mirror point magnetic field strength B_m, which are constant for each row during the electron's drift. The left-most column is the simulated guiding center trajectories for electrons of

different initial conditions in each row. In Figure 2, we also include the field geometry at the two bifurcation points during the electron's drift. The first bifurcation point is when the local B maximum at the equator increases to the level of B_m and the electron starts to bounce within one hemisphere off the equator, and the second bifurcation point is when the local B maximum at the equator drops to the level of B_m and the electron returns to bounce across the equator. These two bifurcation points can also be identified in the trajectory plots on the left-most. These plots in Figure 2 can help illustrate how the second adiabatic invariant changes due to DOB in each case. For example, for case (A) in Figure 1a, the electron has a small initial equatorial pitch angle (with large I_0), thus its B_m is big enough so that the local B maximum at the equator is always smaller than B_m as shown in Figure 2a, leading to no bifurcation and the electron motion is adiabatic. As the initial equatorial pitch angle increases, for example, case (B) in Figure 1a, B_m becomes smaller, and the local B maximum can be bigger than B_m as shown in Figure 2b. This leads to bifurcation as shown in the red line between the 1st and 2nd bifurcation points and the trajectory plot on the left. For this case, the second adiabatic invariant does not change much after the bifurcation, corresponding to the diffusive regime in Figure 1a. However, when the initial equatorial pitch angle is even bigger, and the electron is mirroring near the equator, like case (C) in Figure 1a, the second adiabatic invariant shows a ballistic jump after the bifurcation as shown in Figure 2c. This jump is consistent with the separatrix crossing theory proposed by Cary et al. (1986).

So far, we have discussed the traditional DOB transport in our simulation results that are consistent with previous findings. On the other hand, we find that under certain conditions, electrons can undergo nontraditional DOB transport, which is reported here for the first time. Back to Figure 1, in panel (b), we plot the change of I for electrons with E = 1 MeV, L_{M0} = 7.2, and Kp = 1. In addition to the ballistic, diffusive, and adiabatic regimes of electrons shown by black asterisks

similar to the traditional DOB in panel (a), there are two distinct populations of electrons marked as magenta dots in panel (b), which show different transport in I and are identified as nontraditional DOB transport. Specifically, we find that the electrons marked in magenta include one population of electrons showing diffusive transport with $\langle \Delta I \rangle \approx 0$ in the traditional ballistic regime, and another population showing ballistic transport with $\langle \Delta I \rangle < 0$ in the traditional diffusive regime. These electrons undergoing nontraditional DOB share the same I_0 values as the electrons with traditional DOB but are of different bounce phases, which is interesting. To illustrate the statistical significance of the nontraditional DOB cases, in Figure 1b, we plot the percentage of electrons with nontraditional DOB at each I_0 value in the green curve, with a corresponding y-axis on the right. We see that the percentages of nontraditional DOB cases are generally low, mostly below 20% for all the I_0 values. This explains why the bounce averaged I transport curve in panel (b), the thick red curve, looks similar to that in panel (a) for the pure traditional DOB case, since it is still statistically dominated by the electrons undergoing traditional DOB transport. Therefore, the nontraditional DOB could have a minor effect on the statistically averaged transport of electrons, but its distinct transport is still new and interesting.

To explore the mechanism for the nontraditional DOB transport, we select two cases of electrons marked by (D) and (E) in Figure 1b and plot their evolution of B profiles along the electron drift in Figures 2d and 2e, respectively. The interesting thing we find is that the nontraditional DOB cases are caused by three local B minima of the magnetic field line rather than two local B minima for the traditional cases. The third B minimum near the equator is generally much shallower than the two B minima off the equator, as shown in Figures 2d and 2e. When the electrons are trapped around the third B minimum after the 2nd bifurcation point, its second adiabatic invariant will be

232 small, leading to a diffusive change for electrons with initially small I_0 values (e.g., case (D)) and
233 a ballistic jump for electrons with initially big I_0 values (e.g., case (E)).

234 The three local *B* minima in the magnetic field models have been reported a long time ago (e.g.,
235 Roederer, 1969; Alekseev & Shabansky, 1972), but its effect on the particle drift orbit bifurcations
236 is reported here for the first time. To better illustrate the magnetic field geometry in the T89c
237 magnetic field model, in Figure 3, we trace the magnetic field lines from the magnetic equator
238 from $L = 6$ to 12 on the dayside and plot the number of *B* minima on the GSM x-y plane. The blue
239 area is where field lines are identified with one *B* minimum, the green area is the region with field
240 lines of two local *B* minima, and the red area is for field lines with three local *B* minima. The white
241 area on the dayside at $6 \leq L \leq 12$ are regions with open field lines. Bifurcation can occur in both
242 the red and green areas. Interestingly, results in Figure 3 show that the three local *B* minima regions
243 (red areas) are located between the single *B* minimum and two local *B* minima regions (between
244 blue and green). Moreover, for $Kp = 1$, the red three *B* minima area covers all the transition region
245 from the single *B* minimum to two *B* minima regions (blue to green), which means the electrons
246 must cross the three local *B* minima region before entering the two local *B* minima region. This
247 explains why in Figure 1b at $Kp = 1$, the nontraditional DOB cases due to three *B* minima cover
248 all the I_0 values. While for $Kp = 3$, the results in Figure 3 show that there are regions with no three
249 *B* minima cases in between blue and green, suggesting that for certain values of L_{M0} and I_0 there
250 will be cases with no three *B* minima effects, as shown in the case of Figure 1a. With the
251 distribution of three *B* minima regions shown in Figure 3, we could also expect the nontraditional
252 DOB effects due to three *B* minima to be more significant at larger L_{M0} values and for smaller I_0.
253 This is because particles with smaller second adiabatic invariant or bigger equatorial pitch angle
254 drift further out on the dayside due to the drift shell splitting effect (Roederer, 1967). This Kp, L_{M0},

and I_0 dependence of the three B minima effects on nontraditional DOB is further demonstrated in the simulation results shown in Figure 5, which will be discussed in the next subsection.

3.2 L_M, Kp, and E dependence of the short-term DOB transport

Simulation results in Figure 1 have shown that the short-term transports of electrons due to DOB are distinct under different conditions. Here we further investigate the L_M, Kp, and E dependence of the short-term DOB transport of electrons over one drift. Figure 4 shows the trajectories of 1 MeV electrons on the GSM X-Y plane in the T89c magnetic field model. These electrons are launched at midnight on the equator with ($5 \leq L_{M0} \leq 10$, spacing $\Delta L_{M0} = 0.2$) of 89° equatorial pitch angles and at Kp = 1, 3, 6 respectively in the three panels. The black curves correspond to stably trapped particles, the blue curves indicate bifurcating trajectories, and the green curves are the particles that reach the simulation outer boundary $r = 20\ R_E$ before completing one full drift or quasi-trapped particles. The dashed red circle represents the geosynchronous orbit. The grey areas are the regions with at least two B minima along the field lines, i.e., the green and red areas in Figure 3. Trajectories in Figure 4 show that the bifurcating trajectories (blue curves) or DOB effects move closer to Earth as Kp increases, penetrating inside the geosynchronous orbit for $Kp \geq$ 3, which indicates that DOB can affect a broad region of the outer radiation belt electrons. In addition, the bifurcating trajectories in blue show that the L_M values of electrons can show a big outward jump after one drift. This is corresponding to the jump of I at small I_0 values shown in the ballistic regimes in Figure 1. Since B_m is constant during DOB (conservation of the first adiabatic invariant), a ballistic jump in I value will directly lead to a ballistic jump in L_M, resulting in the outward radial transport of electrons. More analysis on the electron transport in L_M will be discussed in Figure 6 and therein.

To investigate the L_M and Kp dependence of the short-term I transport due to DOB, in Figure 5, we plot the simulation results with different L_{M0} values of L_{M0} = 6.4, 6.8, 7.2, and at different Kp levels of Kp = 1, 3, 6. The format of each panel is the same as in Figure 1. The blue dashed lines separate the ballistic, diffusive, and adiabatic regimes from left to right, with the corresponding values of initial second adiabatic invariants and initial equatorial pitch angles at the boundaries denoted on top. The grey areas are for quasi-trapped electrons which reach r = 20 R_E before completing one full drift, like the green curves in Figure 4. Results in Figure 5 suggest that at a given Kp value, DOB effects are more significant at larger L_{M0}. At Kp = 1, there is no DOB at L_{M0} = 6.4 and 6.8 (consistent with the results in Figure 4), but the traditional and nontraditional DOB transport becomes effective at L_{M0} = 7.2. For Kp = 3 and 6, we see that the I_0 range for DOB effects, i.e., up to the I_0 value of the second blue dash line, is wider as L_{M0} increases. Additionally, the ballistic jump in I due to DOB in the ballistic regime is bigger at higher L_{M0}. Moreover, the simulation results also demonstrate that the DOB transport gets more significant as Kp increases. First, the L_M coverage of DOB approaches closer to Earth at higher Kp values, e.g., DOB is effective at L_{M0} = 6.4 for Kp > 3 but not for Kp = 1. Also, at a given L_{M0}, the ballistic jump in I in the ballistic regime is generally larger as Kp increases. For the nontraditional DOB transport marked in magenta dots, we see that it only affects high L_{M0} region at Kp = 3, which is consistent with the coverage of the three B minima region plotted in Figure 3. Also, the nontraditional DOB effect due to three B minima is more effective at smaller I_0 values (or larger equatorial pitch angles) for Kp = 3 and 6 due to the drift shell splitting effects as discussed in Section 3.1 with Figure 3.

In addition to the electron transport in I, it is also useful to investigate the radial transport of electrons in L_M due to DOB, as shown in the example trajectories in Figure 4. Following the format of Figure 5, we calculate the change of L_M for electrons after one drift at different

conditions and plot the results in Figure 6. The x-axes are identical to Figure 5, but now the y-axis is showing the change in L_M, i.e., $L_{M1} - L_{M0}$, where L_{M1} is the L_M value of the electron after it returns to midnight after one full drift. The thick red curves now represent the bounce-averaged change of L_M, $\langle \Delta L_M \rangle$ with $\Delta L_M = L_{M1} - L_{M0}$, over one drift. Since I has a one-to-one correspondence with L_M due to the constant B_m, the patterns of the radial L_M transport in Figure 6 is similar to those of I transport in Figure 5, showing the same ballistic (with $\langle \Delta L_M \rangle > 0$), diffusive (with $\langle \Delta L_M \rangle \approx 0$), and adiabatic regimes, similar transport due to nontraditional DOB effects, as well as similar L_{M0} and Kp dependence in the transport. It is worthwhile to point out that the jump in L_M due to DOB can be quite significant for high equatorial pitch angle electrons in the ballistic regime, e.g., at $Kp = 3$ with $\langle \Delta L_M \rangle$ reaching ~ 6 R_E at $L_{M0} = 7.2$ and at $Kp = 6$ with $\langle \Delta L_M \rangle$ reaching 4 R_E even closer to Earth at $L_{M0} = 6.4$. This further demonstrates that DOB can play a significant role in the particle transport in the inner magnetosphere.

Even though energy is conserved during the DOB process in a static magnetic field, the electron transport in I and L_M due to DOB can be energy-dependent. Based on the separatrix crossing theory in Cary et al. (1986) and the analytical and numerical calculations in Öztürk and Wolf (2007), the DOB transport is expected to be more significant at higher particle energies, which is related to the energy-dependent gyroradius of electrons at the mirror point. This is consistent with our simulation results shown in Figure 7, which plots the distribution of I_1 after one drift vs. initial I_0 for electrons with $L_{M0} = 7.2$, $Kp = 1$ but at different energies of 1, 2, 4 MeV respectively. The DOB effects are found to be more significant as the energy increases. For example, the ballistic jump in I at small I_0 values is generally larger at higher energies. Also, at a given I_0 value, there is a wider spread in I_1 over different bounce phases as electron energy increases, which is also consistent

with the analytical results in Öztürk and Wolf (2007). Note that the I_0 range over which DOB occurs (up to the second blue dashed line) almost does not change with the electron energy.

3.3 Quantification of the long-term DOB transport

After investigating the short-term DOB transport of electrons after one drift in the previous section, we are motivated to quantify the statistical transport of electrons due to DOB over many drift orbits. We selected three cases in Figure 1a for 1MeV electrons at L_{M0} = 6.8, Kp = 3 but at different I_0 values, one in the ballistic regime (with a small I_0 of 0.0001 R_E), two in the diffusive regime (with I_0 of 0.1 and 0.4 R_E, respectively), and calculate the bounce average squared change of I, $\langle(\Delta I)^2\rangle$, over the drifts, where $\Delta I = I_k - I_0$ and I_k is the second adiabatic invariant of electrons after completing k full drifts. In the first row of Figure 8, we plot the values of $\langle(\Delta I)^2\rangle$ over 20 drift periods for the three selected cases. Similar plots for $\langle(\Delta L_M)^2\rangle$ are shown at the bottom row. The two diffusive cases on the right show a generally linear increase of $\langle(\Delta I)^2\rangle$ and $\langle(\Delta L_M)^2\rangle$ with time, suggesting diffusion over the long term. On the other hand, the ballistic case on the left (with I_0 = 0.0001 R_E) shows a distinctive jump in $\langle(\Delta I)^2\rangle$ and $\langle(\Delta L_M)^2\rangle$ after the first drift, which is consistent with the short-term results. The interesting feature we find is that the ballistic case also illustrates a relatively linear growth over time after the first drift, which will be investigated at the end of this section.

We focus on the diffusive cases first, based on which we could calculate the diffusion coefficients in I as $D_{II} = \langle(\Delta I)^2\rangle/(2\tau)$ and in L_M as $D_{L_ML_M} = \langle(\Delta L_M)^2\rangle/(2\tau)$, where τ is the simulation time longer than a drift period. Specifically, for the diffusive cases in Figure 8, we fit the $\langle(\Delta I)^2\rangle$ and $\langle(\Delta L_M)^2\rangle$ vs. time curves with straight lines over-plotted in red, and half the slope of the fitted red line gives the value of the corresponding diffusion coefficient. This calculation of diffusion

coefficients is then performed for electrons in the diffusive regime of different energies starting at different L_{M0} values and at various Kp levels. The results are shown in Figure 9 for D_{II} and Figure 10 for $D_{L_ML_M}$. One thing we would like to note is that there is no nontraditional DOB transport for the cases shown in Figure 8 for 1 MeV electrons at L_{M0} = 6.8 and Kp = 3, but the nontraditional DOB cases due to three B minima could exist in the diffusive regime, e.g., magenta points in the diffusive regime of Figure 1b. These nontraditional DOB cases, even though non-diffusive in nature, are included in the bounce-averaging of the diffusive coefficient calculation since they are statistically insignificant, as shown in the percentage values in Figure 1b, and will be averaged out statistically.

The calculated results of DOB-induced D_{II} for different electron energies are shown as curves in different colors in Figure 9. The blue dashed lines are the same boundary lines for the diffusive regime as in Figure 5 for 1 MeV electrons. Since the boundary I_0 values between the ballistic and diffusive regimes can change slightly as energy increases, the I_0 coverage of D_{II} for 2 MeV and 4 MeV electrons in blue and red may not align exactly with the blue lines. The grey areas are the same as those in Figure 5 for quasi-trapped electrons. Also as in Figure 5, all the electrons at L_{M0} = 6.4 and 6.8 for Kp = 1 undergo adiabatic motions with no DOB transport. We find that at given L_{M0} and Kp values, the diffusion coefficient D_{II} generally decreases as the equatorial pitch angle decreases for the same electron energy level, and D_{II} is bigger for higher energy electrons at a given I_0. The energy dependence of D_{II} is consistent with the theoretical results in Öztürk and Wolf (2007) because higher energy electrons have bigger gyroradius at the mirror point and shorter drift periods. Comparing across the panels of different L_{M0} and Kp values, the results also show that the DOB-induced D_{II} is generally greater at larger L_{M0} and higher Kp levels. It is of interest to quantify the pitch angle diffusion coefficient, $D_{\alpha\alpha}$, due to DOB, and then compare the DOB-

induced $D_{\alpha\alpha}$ to those caused by other pitch angle diffusion mechanisms such as scattering by chorus waves. Kim et al. (2012) showed that the bounce-averaged $D_{\alpha\alpha}$ due to chorus wave scattering is on the order of about 10^{-2} per day for 1 MeV electrons with $\alpha_{eq} > 45°$ at $L^* = 4.5$ and $Kp = 2$, which is of the same order as or even an order of magnitude smaller than the $D_{\alpha\alpha}$ due to DOB at similar α_{eq} and Kp values even though at high L_{M0}.

The calculated $D_{L_ML_M}$ due to DOB transport, shown in Figure 10, show similar dependence on L_{M0}, Kp, electron energy, and equatorial pitch angle as D_{II}, i.e., higher $D_{L_ML_M}$ at higher electron equatorial pitch angles and energies, and at higher L_{M0} and Kp. To investigate the significance of DOB effects, it is helpful to compare the DOB-induced $D_{L_ML_M}$ with the electron radial diffusion coefficients caused by drift-resonance with ULF waves, even though L_M may not be the same as the L parameters used in various ULF-wave-driven D_{LL} models (ranging from dipole L, McIlwain L (McIlwain, 1961), to L^* (Roederer & Zhang, 2014)). For example, the Brautigam and Albert (2000) magnetic radial diffusion coefficients:

$$D_{LL}^{M}[\text{B\&A}] = 10^{(0.506Kp - 9.325)}L^{10}\ [day^{-1}],\ Kp = 1 \text{ to } 6. \quad (2)$$

at different L (applied using the same value as L_M) and Kp values are plotted as solid black lines in Figure 10. The sum of the magnetic and electric radial diffusion coefficient $D_{LL}^{T}[\text{Ozeke}]$ from Ozeke et al. (2014):

$$D_{LL}^{B} = 6.62 \times 10^{-13}L^{8}10^{-0.0327L^2 + 0.625L - 0.0108Kp^2 + 0.499Kp}\ [day^{-1}], \quad (3)$$

$$D_{LL}^{E} = 2.16 \times 10^{-8}L^{6}10^{0.217L + 0.461Kp}\ [day^{-1}], \quad (4)$$

$$D_{LL}^{T}[\text{Ozeke}] = D_{LL}^{B} + D_{LL}^{E}\ [day^{-1}]. \quad (5)$$

are plotted as dashed black lines. And the dotted black lines are the sum of the magnetic and electric radial diffusion coefficients $D_{LL}^{T}[\text{Ali}]$ from Ali et al. (2016):

$$D_{LL}^{B}[RBSP] = exp\left(a_1 + b_1 \cdot Kp \cdot L^* + L^*\right)\ [day^{-1}], \quad (6)$$

$$D_{LL}^{E}[RBSP] = exp\left(a_2 + b_2 \cdot Kp \cdot L^* + c_2 \cdot L^*\right)\ [day^{-1}], \quad (7)$$

$$D_{LL}^{T}[\mathrm{Ali}] = D_{LL}^{B}[RBSP] + D_{LL}^{E}[RBSP]\ [day^{-1}], \quad (8)$$

where the constants are

$$a_1 = -16.253,\ b_1 = 0.224,$$

$$a_2 = -16.951,\ b_2 = 0.181,\ c_2 = 1.982.$$

All the three empirical models of ULF-wave-driven D_{LL} are shown as single horizontal lines in each panel since they have no energy or pitch angle dependence. By comparing the DOB-driven $D_{L_ML_M}$ with the ULF wave-driven D_{LL}, we see that $D_{L_ML_M}$ could become comparable to the ULF wave-driven D_{LL} at high equatorial pitch angles, and can be even greater than the ULF wave-driven D_{LL} for higher energy electrons at larger L_{M0}, suggesting that DOB could play a significant role in the radial transport of radiation belt electrons.

Quantifying the long-term transport of electrons in the ballistic regime is more challenging than those in the diffusive regime. Based on the short-term transport results in Figures 5 and 6, electrons in the ballistic regime under traditional DOB transport generally jump to a larger I_1 (and L_{M1}) value after the first drift. Then this larger I_1 value (practically the new I_0 value for the second drift) could fall into the diffusive regime and lead to diffusive DOB transport afterward. Then to simulate the long-term transport of electrons in the ballistic regime, it may be adequate to specify the jumps in I and L_M from the first drift orbit and then use the diffusive coefficients derived for the diffusive cases discussed above for subsequent transport. To validate this hypothesis, we examine a ballistic case shown in Figures 8a and 8d for 1 MeV electrons at $L_{M0} = 6.8$, $Kp = 3$ with $I_0 = 0.0001$. Based on the bounce phase averaged red curves in Figures 5e and 6e, after the first drift these electrons

411 will jump to averaged values of $\langle I_1 \rangle \sim 0.3327\ R_E$ and $\langle L_{M1} \rangle \sim 7.2180$, which fall into the diffusive
412 regime according to the simulation results shown in Figures 5f and 6f. Then instead of plotting
413 $\langle (\Delta I)^2 \rangle = \langle (I_k - I_0)^2 \rangle$ over all the drifts as in Figure 8, we calculate and plot $\langle (I_k - \langle I_1 \rangle)^2 \rangle$ over
414 time from after the first drift, as shown in Figure 11a. The curve illustrates a generally linear
415 growth over time, which proves our hypothesis. For a more quantitative comparison, in Figure 11b
416 we plot the $\langle (\Delta I)^2 \rangle = \langle (I_k - I_0)^2 \rangle$ for 1 MeV electrons directly starting from the $I_0 \sim 0.3327\ R_E$
417 and $L_{M0} \sim 7.2180$ at $Kp = 3$ and found that the $\langle (\Delta I)^2 \rangle$ transport is very similar to that of Figure
418 11a. The slight difference is due to the fact that the jump in I and L_M after the first drift can be
419 bounce phase dependent, as shown in the vertical spread in Figures 5 and 6, using the averaged
420 values of $\langle I_1 \rangle$ and $\langle L_{M1} \rangle$ to represent the electron state in I and L_M after the first drift is only
421 approximate and can lead to uncertainties. Nevertheless, our results suggest that the long-term
422 transport of electrons in the ballistic regime could be a combination of advection and diffusion
423 where the electrons undergo ballistic jump in I and L_M after the first drift and then illustrate
424 diffusive transport afterward.

425

426 **4. Conclusions and Discussion**

427 The traditional drift orbit bifurcation (DOB) happens when the dayside magnetosphere is
428 compressed by the solar wind, exhibiting two local magnetic field minima on either side of the
429 equator, i.e., a W-shaped field line. When particles traverse the dayside compressed region, they
430 could be temporarily trapped in one of the hemispheres off the equator when the magnetic field
431 strength at the local maximum at the equator exceeds the magnetic field strength at the particle's
432 mirror points (B_m). The first adiabatic invariant and B_m are constant during DOB, but the second

433 adiabatic invariant I is violated, leading to particle transport in both I and radial distance due to the
434 constant B_m. To better quantify the transport of energetic electrons due to the DOB effects, we use
435 a guiding center test particle code to model the short-term and long-term transport of electrons in
436 I and L_M (equatorial radial distance at midnight) in the T89c magnetic field model under different
437 electron and geomagnetic conditions.

438 The short-term simulation results after one drift show both traditional DOB transport, in which
439 electrons undergo ballistic jumps at large equatorial pitch angles or small I_0 (defined as the ballistic
440 regime), and diffusive transport at bigger I_0 (defined as the diffusive regime), as well as
441 nontraditional DOB transport, in which electrons show diffusive transport in the traditionally
442 defined ballistic regime and ballistic jumps in the traditional diffusive regime. Even though our
443 results show that the nontraditional DOB effects could have a minor effect on the statistically
444 averaged transport of electrons, their distinct transport on electrons is still interesting and is
445 reported here for the first time. Furthermore, we find that the nontraditional DOB cases are caused
446 by three local B minima along the magnetic field line rather than two local B minima for the
447 traditional DOB cases, and their effects are more significant at larger L_{M0} and smaller I_0 values.
448 By further investigating the L_M, Kp, and E dependence of the short-term DOB transport, we find
449 that the DOB effects are more significant at larger L_{M0}, higher Kp, and for electrons of higher
450 energies. The results suggest that DOB can penetrate inside the geosynchronous orbit at $Kp \geqslant 3$,
451 and the jump in L_M due to DOB can be quite significant for high equatorial pitch angle electrons,
452 e.g., with $\langle \Delta L_M \rangle$ reaching 4 R_E at $Kp = 6$ and $L_{M0} = 6.4$. These demonstrate that DOB can play a
453 significant role in the electron transport in the outer radiation belt.

In addition, the long-term DOB transport of electrons is investigated based on our simulation results over many electron drifts. For electrons in the diffusive regime, the diffusion coefficients in I as D_{II} and in L_M as $D_{L_ML_M}$ are calculated, which show higher D_{II} and $D_{L_ML_M}$ at higher electron equatorial pitch angles and energies and at larger L_{M0} and Kp values. Moreover, we find the DOB-induced $D_{\alpha\alpha}$ could be of the same order as or even an order of magnitude higher than the bounce-averaged $D_{\alpha\alpha}$ due to pitch angle diffusion by chorus waves. Please note that the pitch angle diffusion by DOB is drift averaged since it is occurring over the time scale of drifts, while the chorus-induced pitch angle diffusion is bounce averaged. In addition, the DOB-induced $D_{L_ML_M}$ could be comparable to or even higher than the D_{LL} driven by ULF waves at high electron equatorial pitch angles. This suggests that DOB could lead to significant transport of energetic electrons even in the absence of waves, contributing to the fast dropout of radiation belt electrons. Furthermore, the long-term simulation results for electrons in the ballistic regime show that their transport could be approximated as a combination of advection and diffusion where the electrons undergo ballistic jump in I and L_M after the first drift and then diffusive transport afterward. Further validation of this approximation requires detailed comparisons between our test particle simulation results and the simulation results from, e.g., an advection-diffusion model driven by DOB transport rates quantified from the test particle results. Overall, the long-term transport rates of electrons due to DOB quantified in this work are very useful, which could be applied to global radiation belt modeling for studying the relative importance of DOB to the loss and transport of radiation belt electrons.

Finally, we will discuss some potential limitations in our simulation results and the quantified DOB transport. First, for the test particle simulations, we have chosen the T89c magnetic field model since it is solely controlled by the Kp index, which makes it easier to parameterize the

quantified DOB transport rate of electrons as a function of electron and geomagnetic conditions in the future for applications in global radiation belt modeling. However, we are aware that the T89c model may not be as realistic as other magnetic field models, such as the TS04 field model, especially during storm time (Tsyganenko & Sitnov, 2005). But those models are driven by a group of solar wind and geomagnetic parameters and are usually more computationally expensive. Thus, they are more suitable for simulating DOB effects during individual events, which will also be performed in the future. In addition, the three local B minima features that lead to nontraditional DOB transport in our simulation results can be magnetic field model dependent. For example, the three B minima region in the TS04 field model is found to be generally located near the magnetopause boundary right before the open field line region, rather than between the single local B minimum and two local B minima regions, as shown in Figure 3 for the T89c model. In that case, the effects of the nontraditional DOB transport can be less significant. For future event studies of DOB transport using the TS04 model, it will be interesting to investigate the significance of nontraditional DOB cases therein.

Second, since L^* is not defined in DOB, for long-term radial transport of electrons, we have used the L_M parameter and quantified the diffusion coefficient using $D_{L_M L_M}$, which is similar to the approach in Ukhorskiy et al. (2011). Since the global radiation belt models are in adiabatic invariant space (e.g., Tu et al., 2013; Tu, Cunningham, et al., 2014), to obtain a parameter close to the Roederer L^*, Ukhorskiy et al. (2014) calculated a generalized $\bar{L}$ parameter by integrating the magnetic flux over the open drift shells caused by DOB. This $\bar{L}$ parameter, though more computationally expensive to calculate, could be more physical when implementing the parameterized radial diffusion coefficient of electrons due to DOB into global radiation belt

models. Calculation and implementation of this new $\bar{L}$ parameter is also a subject of our future study.

Lastly, other processes, such as field line curvature (FLC) scattering, could also lead to electron transport in static magnetic fields over similar regions as the DOB process. FLC scattering happens when the gyroradius of the particle is comparable to the radius of curvature of the field line. Unlike DOB, FLC scattering violates the first adiabatic invariant of electrons, leading to electron transport in pitch angle (e.g., Tu, Cowee, et al., 2014; Yu et al., 2020). Since we focus on the DOB effects in this work, a guiding-center test particle code is used. However, it is important to recognize that processes such as FLC could violate the guiding-center approximation, especially for higher energy electrons at larger L_M on the nightside. In the future, it is helpful to identify regions that are dominated by either FLC or DOB process and include the electron transport from both processes in global radiation belt models.

Data Availability Statement

The simulation data used in the study are available at https://doi.org/10.5281/zenodo.6796354.

Acknowledgments

This work was supported by the NASA grants 80NSSC18K1284, 80NSSC21K1312, and 80NSSC21K2008, DOE grant DE-SC0020294, and NSF Grant AGS 1752736. The authors would also like to thank Dr. Jay Albert for the insightful discussions about the work.

519 **References**

520 Albert, J. M. (2014). Radial diffusion simulations of the 20 September 2007 radiation belt
521 dropout. *Annales de Geophysique, 32*(8), 925-934. https://doi.org/10.5194/angeo-32-925-
522 2014

523 Alekseev, I. I., Shabansky, V. P. (1972). A model of a magnetic field in the geomagnetosphere.
524 *Planetary and Space Science 20*, 117–133. https://doi.org/10.1016/0032-0633(72)90146-8

525 Ali, A. F., Malaspina, D. M., Elkington, S. R., Jaynes, A. N., Chan, A. A., Wygant, J., &
526 Kletzing, C. A. (2016). Electric and magnetic radial diffusion coefficients using the Van
527 Allen probes data. *Journal of Geophysical Research: Space Physics*, *121*, 9586–9607.
528 https://doi.org/10.1002/2016JA023002

529 Allen, J. (2010). The galaxy 15 anomaly: Another satellite in the wrong place at a critical time.
530 *Space Weather, 8*(6). https://doi.org/10.1029/2010SW000588

531 Baker, D. N. (2001). Satellite anomalies due to space storms. In Space storms and space weather
532 hazards (pp. 285-311). The Netherlands: Springer. https://doi.org/10.1007/978-94-010-0983-
533 6_11

534 Baker, D. N., & Kanekal, S. (2008). Solar cycle changes, geomagnetic variations, and energetic
535 particle properties in the inner magnetosphere. *Journal of Atmospheric and Solar-Terrestrial*
536 *Physics*, *70*, 195-206. https://doi.org/10.1016/j.jastp.2007.08.031

537 Brautigam, D. H., & Albert, J. M. (2000). Radial diffusion analysis of outer radiation belt
538 electrons during the October 9, 1990, magnetic storm, *Journal of Geophysical Research,*
539 *Space Physics*, *105*(A1), 291-309. https://doi.org/10.1029/1999ja900344

Brizard, A. J., & Chan, A. A. (1999). Nonlinear relativistic gyrokinetic Vlasov-Maxwell equations, *Physics of Plasmas*, 6, 4548. https://doi.org/10.1063/1.873742

Cary, J. R., Escande, D. F., & Tennyson, J. L. (1986). Adiabatic-invariant change due to separatrix crossing, *Physical Review Letters*, *34*(5), 4256-4275. https://doi.org/10.1103/PhysRevA.34.4256

Fälthammar, C.-G. (1965). Effects of time-dependent electric fields on geomagnetically trapped radiation, *Journal of Geophysical Research*, *70*(11), 2503–2516. https://doi.org/10.1029/JZ070i011p02503

Kim, K.-C., Shprits, Y., Subbotin, D., & Ni, B. (2012). Relativistic radiation belt electron responses to GEM magnetic storms: Comparison of CRRES observations with 3-D VERB simulations. *Journal of Geophysical Research*, *117*, A08221. https://doi.org/10.1029/2011JA017460

McIlwain, C. E. (1961). Coordinates for mapping the distribution of magnetically trapped particles. *Journal of Geophysical Research*, *66*(11), 3681–3691. https://doi.org/10.1029/JZ066i011p03681

Ozeke, L. G., Mann, I. R., Murphy, K. R., Jonathan Rae, I., & Milling, D. K. (2014). Analytic expressions for ULF wave radiation belt radial diffusion coefficients. *Journal of Geophysical Research: Space Physics, 119*, 1587–1605. https://doi.org/10.1002/2013JA019204

Ozeke, L. G., Mann, I. R., Murphy, K. R., Sibeck, D. G., & Baker, D. N. (2017). Ultra-relativistic radiation belt extinction and ULF wave radial diffusion: Modeling the September

2014 extended dropout event, *Geophysical Research Letters*, *44*(6), 2624-2633. https://doi.org/10.1002/2017GL072811

Öztürk, M. K., & Wolf, R. A. (2007). Bifurcation of drift shells near the dayside magnetopause. *Journal of Geophysical Research*, *112*(A7), A07207.https:// doi.org/10.1029/2006JA012102

Reeves, G. D., McAdams, K. L., Friedel, R. H. W., & O'Brien, T. P. (2003). Acceleration and loss of relativistic electrons during geomagnetic storms, *Geophysical Research Letters*, *30*(10), 1529. https://doi.org/10.1029/2002GL016513

Roederer, J. G. (1967). On the adiabatic motion of energetic particles in a model magnetosphere. *Journal of Geophysical Research* (1896-1977), *72*(3),981–992. https://doi.org/10.1029/JZ072i003p00981

Roederer, J. G. (1969). Quantitative models of the magnetosphere. *Reviews of Geophysics*, *7*, 77–96. https://doi.org/10.1029/RG007i001p00077

Roederer, J. G. (1970). Dynamics of geomagnetically trapped radiation. In J. G. Roederer & J. Zahringer (Eds.), *Physics and chemistry in space* Vol. (2), Springer. https://doi.org/10.1007/978-3-642-49300-3

Roederer, J. G., & Zhang, H. (2014). *Dynamics of magnetically trapped particles: foundations of the physics of radiation belts and space plasmas.* Astrophysics and space science library, Springer. https://doi.org/10.1007/978-3-642-41530-2

Thorne, R. M. (2010). Radiation belt dynamics: The importance of wave-particle interactions. *Geophysical Research Letters*, *37*, L22107. https://doi.org/10.1029/2010GL044990

Thorne, R. M., Li, W., Ni, B., Ma, Q., Bortnik, J., Chen, L., et al. (2013). Rapid local acceleration of relativistic radiation-belt electrons by magnetospheric chorus. *Nature*, *504*(7480), 411–414. https://doi.org/10.1038/nature12889

Tsyganenko, N. A. (1989). A magnetospheric magnetic field model with a warped tail current sheet. *Planetary and Space Science*, *37*, 5–20. https://doi.org/10.1016/0032-0633(89)90066-4

Tsyganenko, N. A., & Sitnov, M. I. (2005). Modeling the dynamics of the inner magnetosphere during strong geomagnetic storms. *Journal of Geophysical Research*, *110*, A03208. https://doi.org/10.1029/2004JA010798

Tu, W., Cowee, M. M., & Liu, K. (2014). Modeling the loss of inner belt protons by magnetic field line curvature scattering. *Journal of Geophysical Research: Space Physics*, 119(7), 5638–5650. https://doi.org/10.1002/2014JA019864

Tu, W., Cunningham, G. S., Chen, Y., Henderson, M. G., Camporeale, E., & Reeves, G. D. (2013). Modeling radiation belt electron dynamics during GEM challenge intervals with the DREAM3D diffusion model. *Journal of Geophysical Research: Space Physics*, *118*(10), 6197–6211. https://doi.org/10.1002/jgra.50560

Tu, W., Cunningham, G. S., Chen, Y., Morley, S. K., Reeves, G. D., Blake, J. B., et al. (2014). Event-specific chorus wave and electron seed population models in DREAM3D using the Van Allen Probes. *Geophysical Research Letters*, *41*, 1359–1366. https://doi.org/10.1002/2013GL058819

599 Turner, D. L., Shprits, Y., Hartinger, M., & Angelopoulos, V. (2012). Explaining sudden losses
600 of outer radiation belt electrons during geomagnetic storms. *Nature Physics*, *8*(3), 208–212.
601 https://doi.org/10.1038/nphys2185

602 Ukhorskiy, A. Y., Sitnov, M. I., Millan, R. M., & Kress, B. T. (2011). The role of drift orbit
603 bifurcations in energization and loss of electrons in the outer radiation belt. *Journal of*
604 *Geophysical Research*, *116*(A9), A09208. https://doi.org/10.1029/2011JA016623

605 Ukhorskiy, A. Y., Sitnov, M. I., Millan, R. M., Kress, B. T., & Smith, D. C. (2014). Enhanced
606 radial transport and energization of radiation belt electrons due to drift orbit bifurcations.
607 *Journal of Geophysical Research: Space Physics*, *119*(1), 163–170.
608 https://doi.org/10.1002/2013JA019315

609 Ukhorskiy, A. Y., Sitnov, M. I., Millan, R. M., Kress, B. T., Fennell, J. F., Claudepierre, S. G., &
610 Barnes, R. J. (2015). Global storm time depletion of the outer electron belt. *Journal of*
611 *Geophysical Research: Space Physics*, *120*(4), 2543–2556.
612 https://doi.org/10.1002/2014ja020645

613 Wan, Y., Sazykin, S., Wolf, R. A., & Öztürk, M. K. (2010). Drift shell bifurcation near the
614 dayside magnetopause in realistic magnetospheric magnetic fields. Journal of Geophysical
615 Research: Space Physics, 115(A10), A10205. https://doi.org/10.1029/2010JA015395

616 Yu, Y., Tian, X., & Jordanova, V. K. (2020). The effects of field line curvature (FLC) scattering
617 on ring current dynamics and isotropic boundary. *Journal of Geophysical Research: Space*
618 *Physics*, *125*, e2020JA027830. https://doi.org/10.1029/2020JA027830

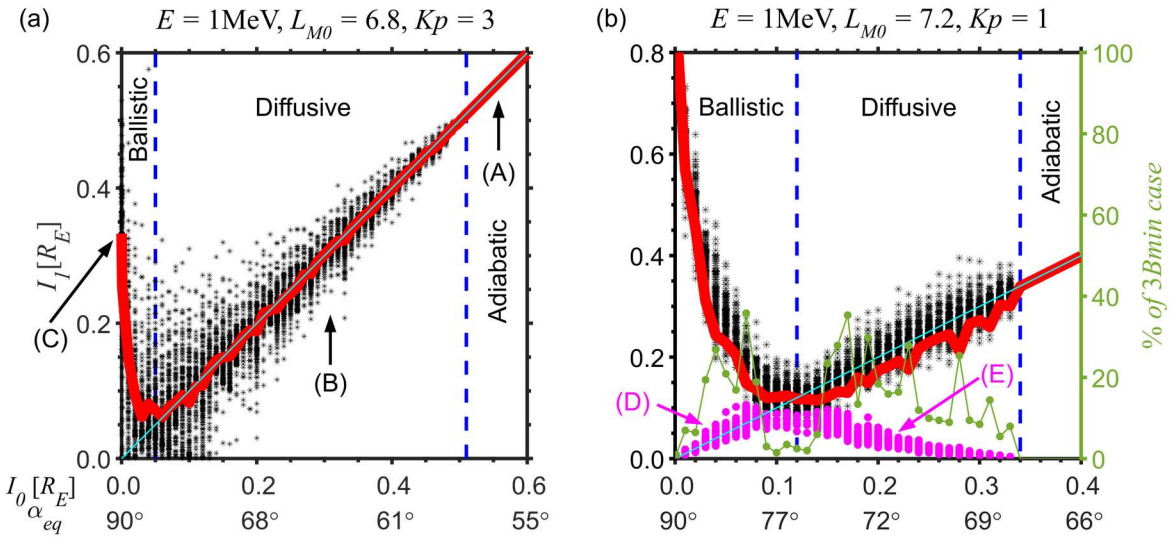

Figure 1. Distribution of the second adiabatic invariant after one drift for 1 MeV electrons starting from (a) $L_{M0} = 6.8$ at $Kp = 3$, and (b) $L_{M0} = 7.2$ at $Kp = 1$. The x-axes are the initial second adiabatic invariant values with corresponding initial equatorial pitch angles shown below. Left y-axes are the second adiabatic invariant values after one drift. The right y-axis of panel (b) is the percentage of the 3Bmin cases. The blue dashed lines are the boundaries for ballistic, diffusive, and adiabatic regimes. Marks (A)-(E) denote the different cases of electrons shown in Figure 2.

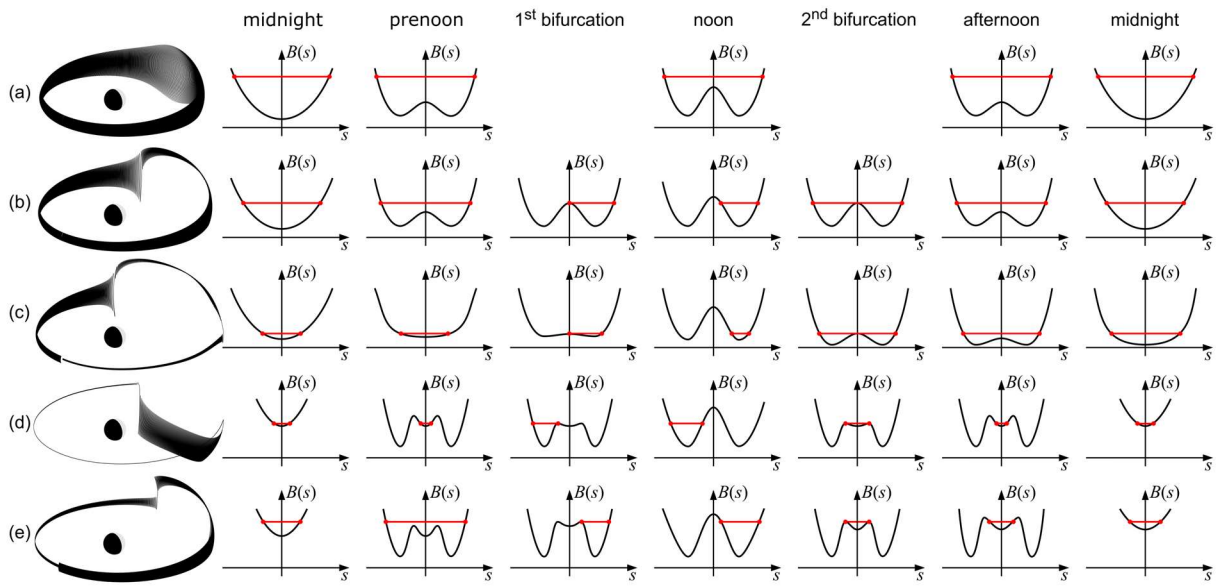

626

627 **Figure 2.** Traditional and nontraditional DOB illustration with simulated particles' trajectories on
628 the left-most and sketched B profiles along the drift on the right. (a-e) correspond to cases of (A-
629 E) in Figure 1. The x-axis is the distance along the magnetic field line, and the y-axis is the
630 magnetic field magnitude. The red lines are B_m values which are constant along the electron drift.

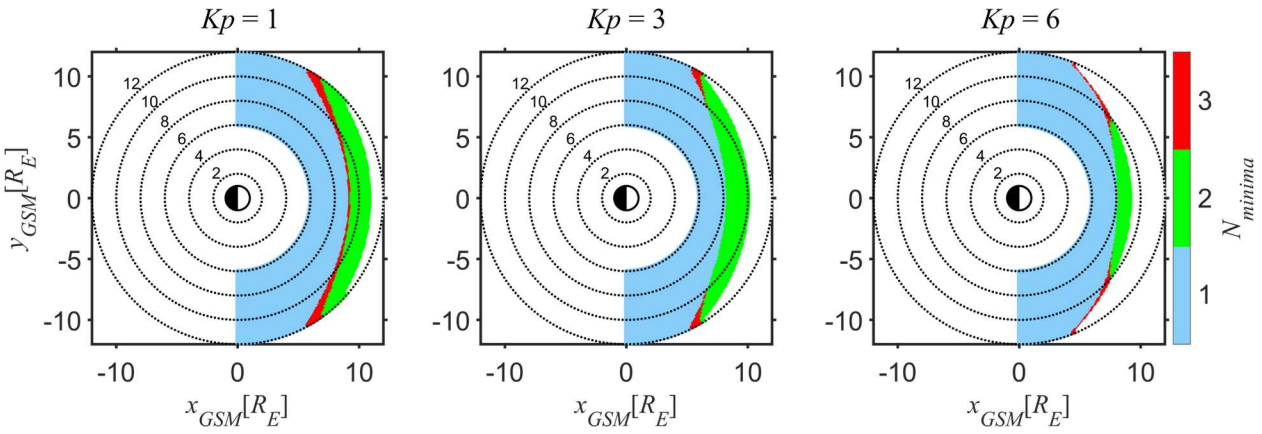

Figure 3. Number of magnetic field minima for field lines crossing the magnetic equator between $L = 6$ and $L = 12$ on the dayside for the T89c magnetic field model at (a) $Kp = 1$, (b) $Kp = 3$ (b), and (c) $Kp = 6$. Blue, green, and red areas are regions with field lines of one, two, and three local B minima, respectively. The white area on the dayside inside $6 \leq L \leq 12$ are regions with open field lines.

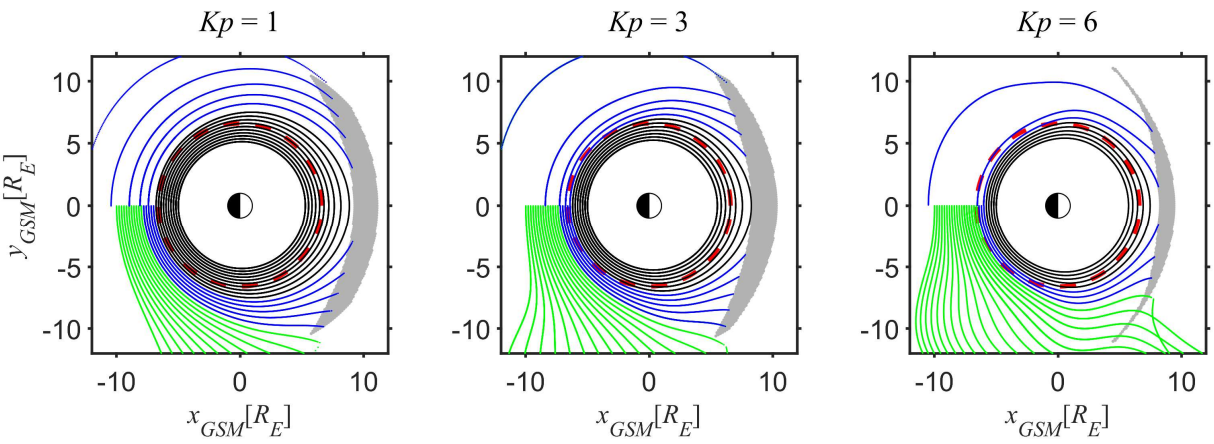

637

638 **Figure 4**. Trajectories of electrons starting from $5 < L_{M0} < 10$ with $\Delta L_{M0} = 0.2$ on the midnight
639 magnetic equator with 89° equatorial pitch angle at (a) Kp =1 (a), (b) Kp = 3, and (c) Kp = 6. The
640 black curves represent the stably trapped electrons. The blue curves are bifurcated drift shells. The
641 green curves indicate the quasi-trapped electrons, which reach r = 20 R_E before completing one
642 full drift. The grey area on the right for each panel is the region with two or three local B minima
643 along the field lines, corresponding to the red and yellow areas in Figure 3. The dashed red circle
644 is the geosynchronous orbit.

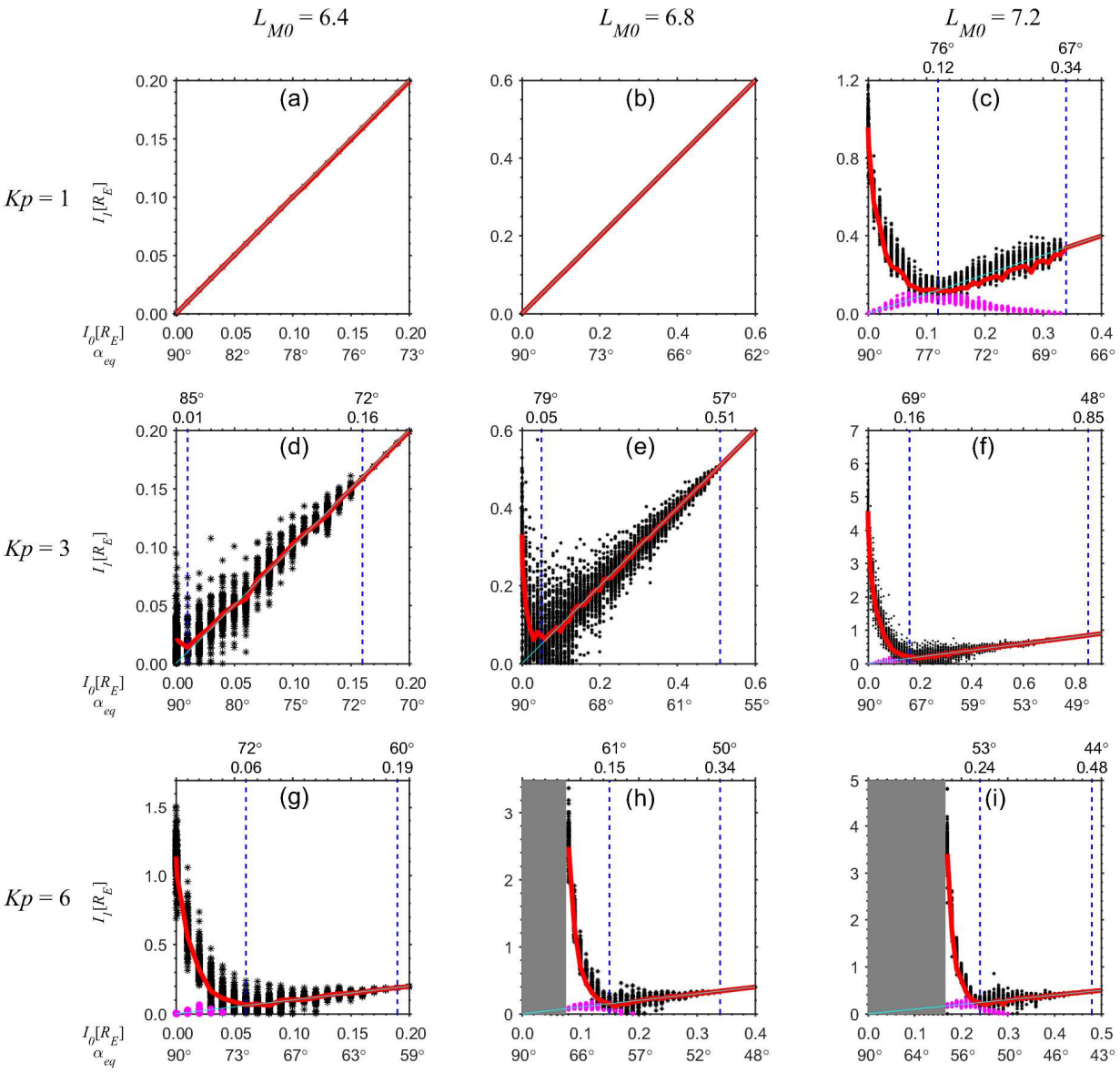

645

646 **Figure 5**. Same format as Figure 1 but for Kp = 1 (a-c), Kp = 3 (d-f), Kp = 6 (g-i), and L_{M0} = 6.4
647 (a, d, g), L_{M0} = 6.8 (b, e, h), L_{M0} = 7.2 (c, f, i). The values above the dashed blue lines are the
648 corresponding values of initial second adiabatic invariants and initial equatorial pitch angles at the
649 boundaries.

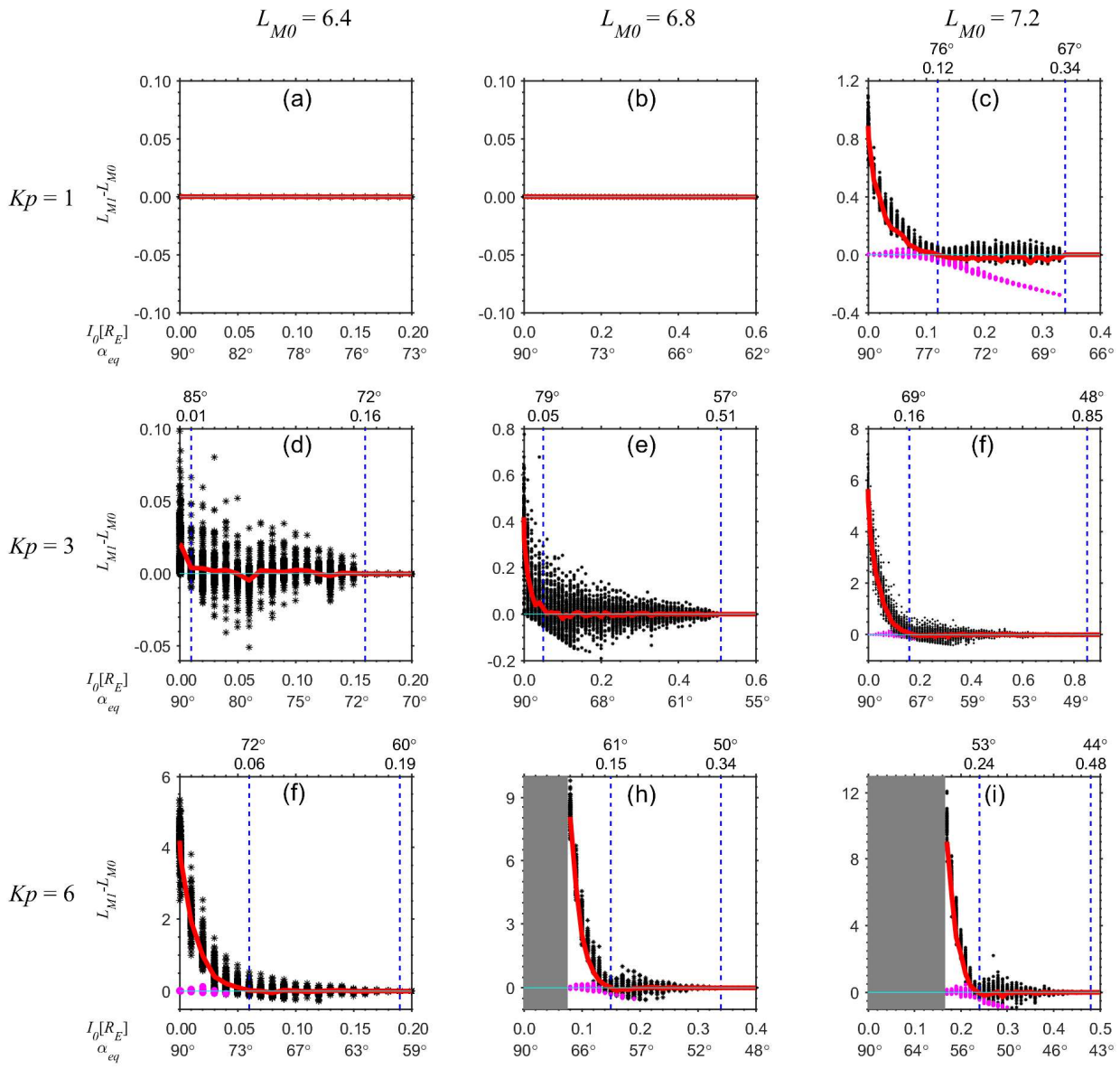

Figure 6. Same format as Figure 5, but with y-axis showing the change of L_M after one full drift.

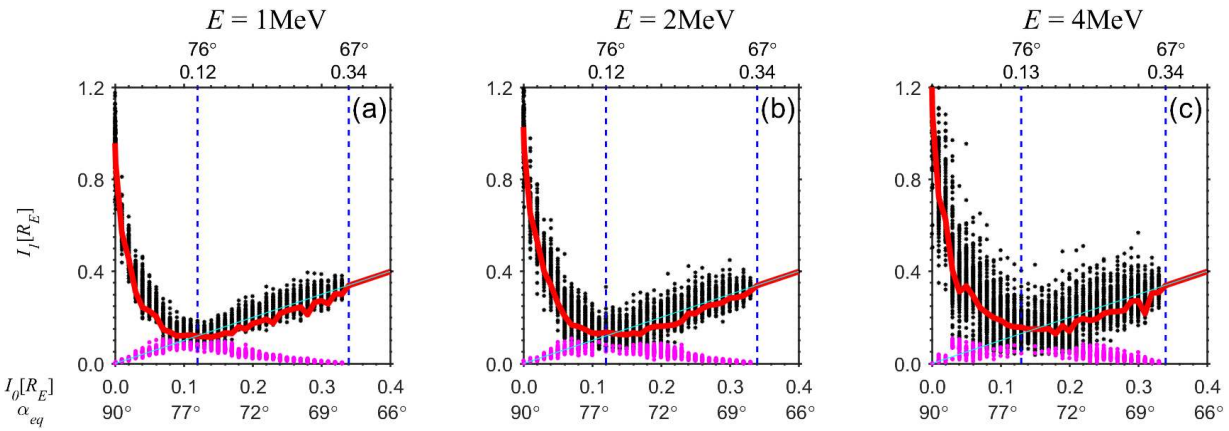

652

653 **Figure 7**. Same format as Figure 1b for L_{M0} = 7.2 and Kp = 1, but for electrons at E = 1, 2, and 4

654 MeV respectively in panels (a), (b), and (c).

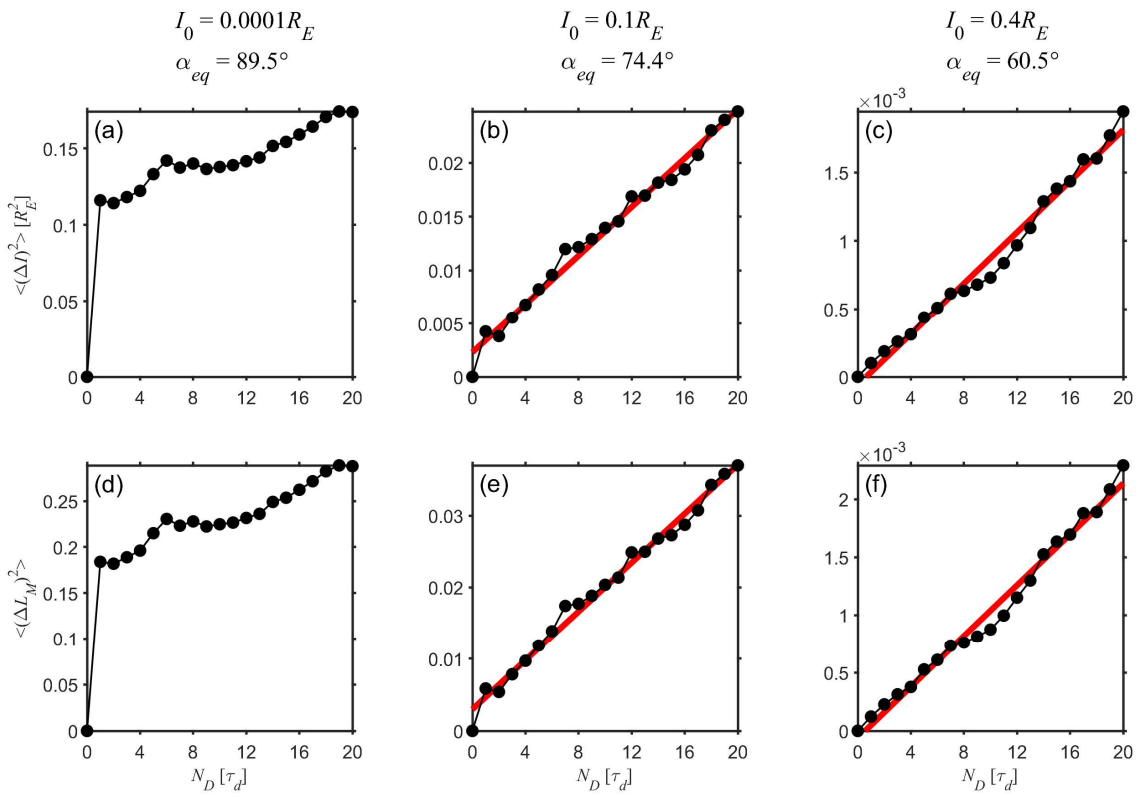

655

656 **Figure 8**. Average squared change of the second adiabatic invariant (a, b, c) and L_M over 20 drift
657 periods for 1 MeV electrons at L_{M0} = 6.8, Kp = 3 but with different initial second adiabatic
658 invariants, 0.0001 (a, d), 0.1 (b, e), and 0.4 R_E (c, f) with corresponding equatorial pitch angle
659 values denoted below. The red lines in (b, c, e, f) are lines of best fit.

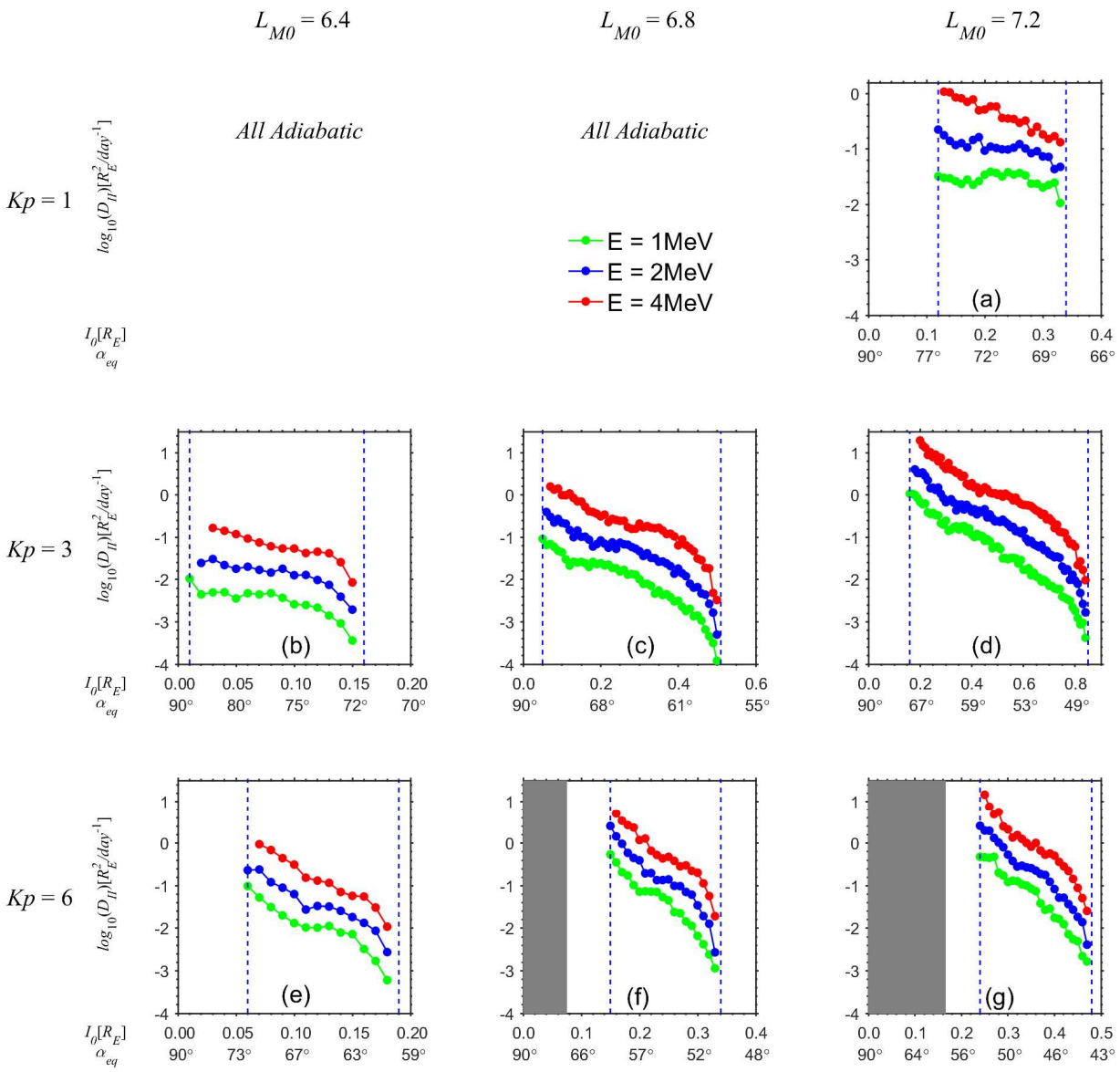

Figure 9. Diffusion coefficients in the second adiabatic invariant, D_{II}, due to DOB at Kp = 1 (top), Kp = 3 (middle), Kp = 6 (bottom), and L_{M0} = 6.4 (left), L_{M0} = 6.8 (middle), L_{M0} = 7.2 (right), for electrons at E = 1 (green), 2 (blue), and 4 MeV (red). The x-axes are the initial second adiabatic invariant values, and the y-axis is the log value of D_{II}.

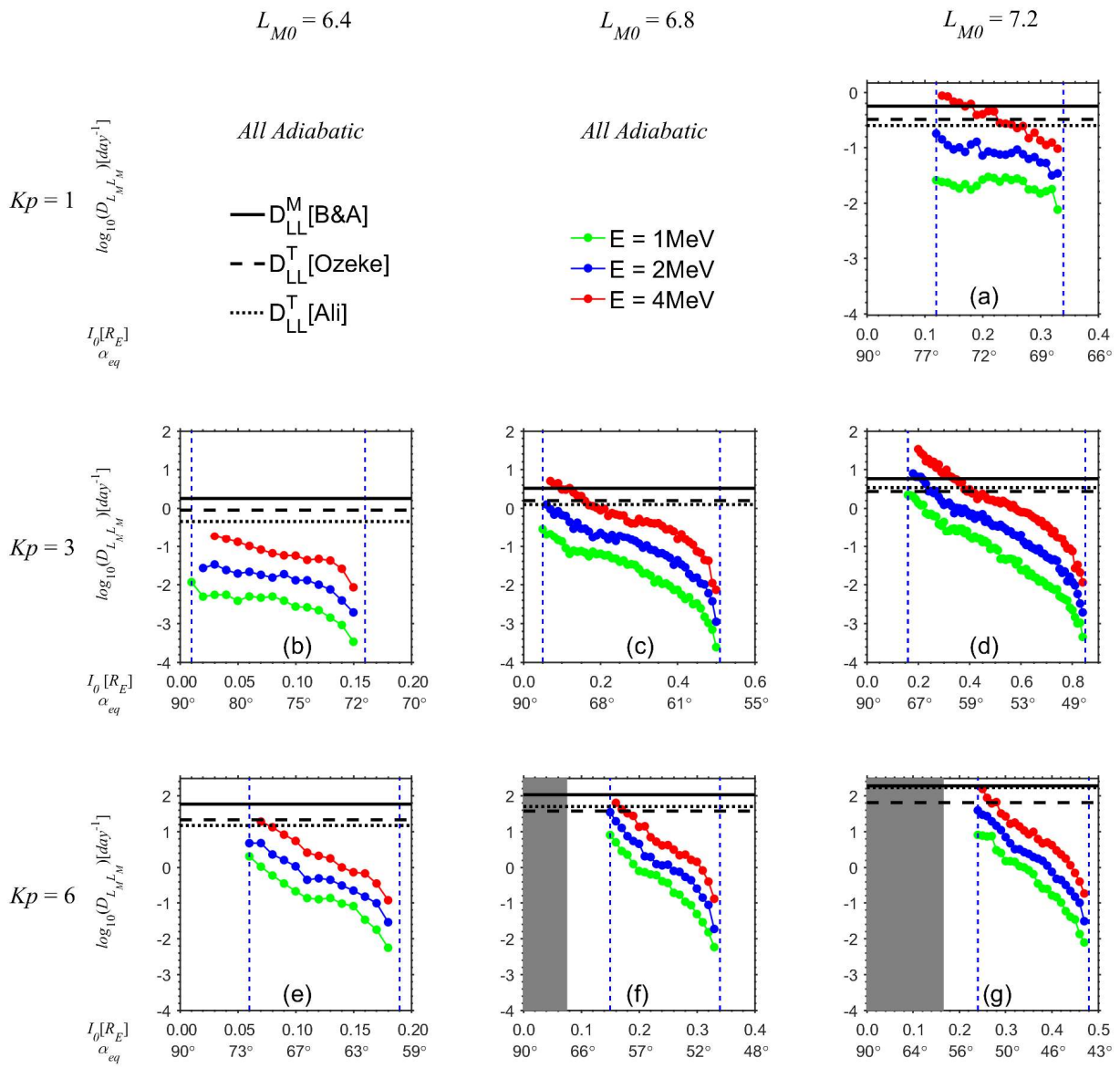

665

666 **Figure 10.** Same format as Figure 9, but for the diffusion coefficient of the L_M due to DOB with

667 the y-axis being the log value of $D_{L_M L_M}$. The solid, dashed, and dotted black lines are D^{M}_{LL}[B&A],

668 D^{T}_{LL}[Ozeke], and D^{T}_{LL}[Ali], respectively.

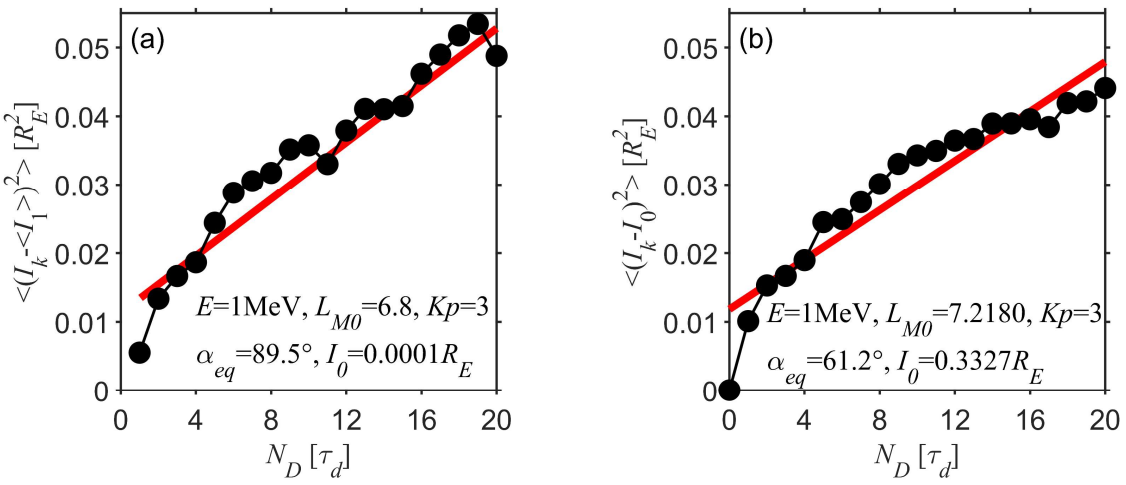

669

670 **Figure 11**. Same format as Figure 8, but the y-axis in panel (a) showing the values of $\langle (I_k - \langle I_1 \rangle)^2 \rangle$

671 after the first drift.